J. Fluid Mech. (2003), *vol.* 481, *pp.* 77–104.
DOI: 10.1017/S0022112002003592 Printed in the United Kingdom

A singularity method for calculating time-dependent viscoelastic flows with integral constitutive equations

By RONALD J. PHILLIPS

Department of Chemical Engineering and Materials Science, University of California, Davis, Davis, CA 95616, USA

(Received 21 September 2001 and in revised form 18 October 2002)

A new method is introduced for calculating time-dependent, non-Newtonian flows of fluids described by integral constitutive equations. The starting point for the method is the integral form of the solution to the equations of motion, valid in the limit of low Reynolds number. Because of the non-Newtonian nature of the fluid, this solution includes an integral over the domain of the flow, which is not present in boundary integral methods. This integral over the fluid volume (in three dimensions) or area (in two dimensions) is converted to a Lagrangian reference frame, and discretized for numerical evaluation. Because points in the integrand move with the fluid velocity, values of the non-Newtonian portion of the stress can be found by integrating the deformation at those points in conjunction with a suitable integral constitutive equation. The contribution to the total velocity field of the non-Newtonian stress at each fluid element is that of a point dipole, and the method bears many similarities to the point-vortex method for calculating inviscid flows. Like the point-vortex method, it is necessary to introduce cutoff functions that remove the singular nature of the dipole–dipole interactions. In addition, to render the method computationally feasible, the interactions between the dipoles must be calculated by the fast-multipole method or some comparable approach. Methods for calculating cutoff functions and implementing the fast multipole method are discussed, and simulation results are presented for one- and two-phase time-dependent flows of viscoelastic fluids between eccentric and concentric rotating cylinders.

1. Introduction

In the context of low Reynolds number flow, a 'singularity method' is a method of obtaining solutions to problems in terms of a sum of contributions from point forces, point dipoles and higher-order multipoles. In Newtonian fluids, singularity methods, which are closely related to boundary-integral methods, involve placing a collection or distribution of these so-called image singularities in a region exterior to the flow, and assigning their strengths and positions such that they yield the appropriate boundary conditions (Pozrikidis 1992). This approach has been used, for example, to calculate flow around axisymmetric bodies, and hydrodynamic interactions between suspended ellipsoidal particles (Chwang & Wu 1975; Kim 1986), and is also an important component of slender-body theory (Batchelor 1970; Cox 1970). It bears an obvious similarity to the method of images used in electrostatics (Jackson 1975; Phillips 1995), and provides elegant and simple solutions to some problems, particularly those involving the motion and interactions of suspended particles. In this paper, we show

how such a method can be used to calculate time-dependent viscoelastic flows of fluids described by integral constitutive equations.

As noted by Rajagopalan, Armstrong & Brown (1993), an important advantage of integral models is the relative ease and efficiency with which they can model distributions of relaxation times. It is also noteworthy that some of the best models for capturing the rheological behaviour of polymeric liquids over a range of steady and time-dependent conditions are of the integral type. For example, the Kaye–Bernstein–Kearsley–Zapas or KBKZ model remains one of the best in providing quantitative agreement with rheological data (Tanner 1992). However, identifying accurate and efficient numerical methods to use with such integral models has been problematic. To date, two methods have been introduced for calculating time-dependent flows with integral constitutive equations (Rasmussen 1999; Peters, Hulsten & van den Brule 2000). The current method differs from both of those significantly, particularly in the absence of either a fixed or Lagrangian mesh. It is therefore plausible that singularity or integral methods such as this one will provide a convenient alternative technique for some problems, particularly those with complicated time-dependent geometries.

A numerical form of a singularity method was proposed by Dabros (1985), who suggested that the singularities be located in some regular configuration, and that their strengths be calculated by minimizing the deviation from conditions specified at the boundaries. This idea has since been used by others to examine the behaviour of particles in wavy-walled tubes (Nitsche & Brenner 1990), fibrous matrices (Clague & Phillips 1996; 1997) and Brinkman media (Buck, Dungan & Phillips 1999). A significant extension of the approach, to model non-neutrally buoyant Newtonian drops with surface tension, was recently reported by Nitsche & Schaflinger (2001). Here a singularity method is developed for calculating viscoelastic flows by using, in addition to singularities external to the flow, point dipoles that are distributed throughout the fluid itself.

This approach can be motivated physically by consideration of the bead-and-spring dumbbells commonly used in kinetic-theory models of polymer solutions. The velocity disturbance $\boldsymbol{v}'$ of a bead-and-spring dumbbell with beads at positions $\boldsymbol{x}_1$ and $\boldsymbol{x}_2$ is given by

$$\boldsymbol{v}'(\boldsymbol{x}) = \frac{1}{4\pi\mu}[\boldsymbol{J}(\boldsymbol{x}-\boldsymbol{x}_1)\cdot\boldsymbol{F} - \boldsymbol{J}(\boldsymbol{x}-\boldsymbol{x}_2)\cdot\boldsymbol{F}], \tag{1}$$

where $\boldsymbol{F}$ is the force exerted on the beads by the spring, μ is the viscosity of the suspending fluid, and $\boldsymbol{J}$ is the point-force propagator, or singular solution to Stokes equations. In the continuum limit, where $\boldsymbol{x}_1 - \boldsymbol{x}_2 \to 0$, a Taylor expansion shows that

$$\boldsymbol{v}'(\boldsymbol{x}) = \frac{1}{4\pi\mu}\Delta\boldsymbol{x}\cdot\nabla\boldsymbol{J}(\boldsymbol{x}-\boldsymbol{x}')\cdot\boldsymbol{F} = \frac{1}{4\pi\mu}\boldsymbol{D}:\nabla\boldsymbol{J}, \tag{2}$$

where the dipole $\boldsymbol{D}$ is defined by $\boldsymbol{D} = \Delta\boldsymbol{x}\boldsymbol{F}$ and $\boldsymbol{x}'$ is its location. The fact that the dipole strength per unit volume of fluid is the same as Kramer's expression for the dumbbell contribution to the stress (Bird *et al.* 1987*b*) indicates that, in the continuum limit, non-Newtonian stresses may be represented as a distribution of point dipoles, which contribute a velocity disturbance given by (2). A mathematical derivation of this result, which is based on the integral form of the solution for the flow and is valid for any constitutive equation, is provided in § 2. Note that $\Delta\boldsymbol{x}$ and $\boldsymbol{F}$ are both oriented along the bead-to-bead axis, guaranteeing that the dipole $\boldsymbol{D}$ is symmetric.

Direct simulations of the flow of suspensions of bead-and-spring dumbbells were performed by Binous & Phillips (1999*a*, *b*). In such simulations, the strength of

the velocity disturbance contributed by a dumbbell is determined by the force the springs exert on the beads, which are pushed apart by spatial variations in the velocity field, as well as by Brownian motion. Because a dipole is located at a single point, in a simulation involving these point singularities, their strengths do not evolve as a necessary component of the simulation, but must be evaluated by making use of constitutive equations. Here we make use of integral constitutive equations, which describe the stress in a fluid element in terms of the deformation it has experienced during a history spanning many relaxation times. Because such equations are written in a Lagrangian reference frame, they coordinate naturally with an integral representation of the solution in which integrals over the flow domain are written in a Lagrangian frame of reference. The dipole positions are advanced in time according to the fluid velocity, with each dipole contributing the non-Newtonian portion of the stress in its own fluid element.

One difficulty with the point-dipole method (PDM) used here lies in the fact that the dipoles, which are constantly in motion and interact with each other, are singular. Without a suitable method for smoothing the dipole–dipole interactions, the time evolution of a flow containing such singular entities can become unstable. A very similar challenge is present with the point-vortex method for calculating inertia-dominated flows (Puckett 1993). In that approach, the equations of motion are expressed in terms of the vorticity, and the solution involves summing contributions of singular point vortices that move with the fluid velocity, just as the dipoles do in the point-dipole method. The point vortices and point dipoles are mathematically very similar, and for both methods so-called 'cutoff' functions can be derived that remove the singular interaction at small separations, stabilizing the system. Error estimates for this smoothing process can also be derived, and are discussed below.

In order to make the point–dipole method computationally efficient, it is also necessary to sum the dipole–dipole interactions rapidly and accurately. If performed in the most straightforward way, the computation time for such a sum is $O(N^2)$, where N is the number of dipoles. However, the fast multipole method (FMM) of Greengard (1988) and Greengard & Rokhlin (1997) provides an algorithm for reducing the rate of growth in computation time to $O(N)$, providing an enormous saving in calculations which can involve 10^5 dipoles. The FMM has been used most widely to calculate electrostatic interactions. However, it has also been used by Sangani & Mo (1996) to calculate low-Reynolds-number hydrodynamic interactions in Newtonian flows. An approach modified to suit the PDM is used here. A growing literature attests to the efficacy of parallel versions of the FMM (Greengard & Gropp 1990; Board *et al.* 1992; Lee & Jeong 1998; Choi, Ruedenberg & Gordon 2001), a fact which will make large-scale multipole-based simulations feasible on parallel computers or computer clusters.

We have chosen the flow between eccentric rotating cylinders, or the journal-bearing problem, as a convenient geometry for a preliminary evaluation of the point-dipole method. As shown in figure 1, the radii of the inner and outer cylinders are R_i and R_0, respectively, and the inner cylinder rotates with angular velocity Ω in the z-direction. In the limit where the gap between the two cylinder surfaces is small relative to the radius, asymptotic results are available for quantitative comparison with the numerical results obtained here (Ballal & Rivlin 1976; Phan-Thien & Tanner 1981; Beris, Armstrong & Brown 1983). These results pertain to low Deborah numbers, or $De \ll 1$, where De is given by

$$De = \Omega\lambda, \tag{3}$$

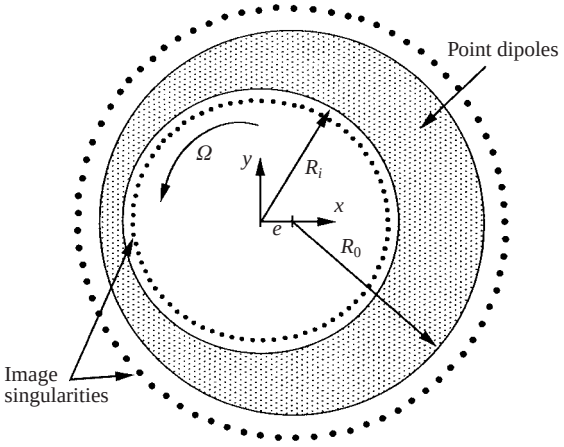

FIGURE 1. Schematic diagram of eccentric cylinders with centres separated by a distance e in the x-direction. The inner cylinder rotates with rotational velocity Ω in the z-direction, and the flow is in the annulus between the cylinders. Solid circles outside the flow domain are image singularities (point forces and dipoles).

and is the ratio of the fluid relaxation time λ to the time for a fluid element to circulate around the gap in the θ-direction. However, in some cases the Weissenberg number Wi, defined by

$$Wi = \frac{\Omega \lambda R_i}{R_0 - R_i}, \tag{4}$$

can be of order unity. As the product of λ and a characteristic shear rate, it is Wi that determines the strength of the normal stresses in the flow. Hence, this test problem can be used to evaluate the efficacy of the PDM in calculating normal stresses, in addition to shear-thinning and transient behaviour in viscoelastic flows.

2. Description of the problem

As shown in figure 1, we consider a system of eccentric cylinders, with the inner cylinder rotating and the outer one stationary. The origin is placed at the centre of the inner cylinder, and is displaced by a distance $-e$ in the x-direction from the centre of the outer cylinder. We define a dimensionless gap distance δ as

$$\delta = \frac{R_0 - R_i}{R_i} \tag{5}$$

and a dimensionless eccentricity ε by

$$\varepsilon = \frac{e}{R_0 - R_i}. \tag{6}$$

Also shown schematically in figure 1 are singularities external to the flow and point dipoles in the fluid. The latter create velocity disturbances as given by (2) with

$$\boldsymbol{J}(\boldsymbol{x}) = -\boldsymbol{I} \ln(r) + \frac{\boldsymbol{x}\boldsymbol{x}}{r^2}, \tag{7}$$

where $r = |\boldsymbol{x}|$.

Under conditions where inertial effects are negligible, the equations governing conservation of mass and momentum in the incompressible fluid are

$$\nabla \cdot \boldsymbol{v} = 0 \tag{8}$$

and

$$\nabla \cdot \boldsymbol{\tau} - \nabla p = -\nabla \cdot \boldsymbol{\tau}^p, \tag{9}$$

where $\boldsymbol{v}$ and p are the fluid velocity and pressure, respectively, and no-slip conditions are imposed on $\boldsymbol{v}$ on both cylinder surfaces. The stress tensor $\boldsymbol{\sigma}$ is given by $\boldsymbol{\sigma} = -p\boldsymbol{I} + \boldsymbol{\tau} + \boldsymbol{\tau}^p$, where the Newtonian stress $\boldsymbol{\tau}$ is related to the rate of strain tensor $\dot{\boldsymbol{\gamma}}$ and the velocity $\boldsymbol{v}$ by

$$\boldsymbol{\tau} = \mu\dot{\boldsymbol{\gamma}} = \mu(\nabla \boldsymbol{v} + \nabla \boldsymbol{v}^t). \tag{10}$$

Here μ is a constant Newtonian viscosity, and all non-Newtonian stresses are represented by the stress tensor $\boldsymbol{\tau}^p$.

We represent the viscoelastic portion of the stress by either of two well-known integral constitutive equations. The first,

$$\boldsymbol{\tau}^p = (S\eta_0 - \mu)\dot{\boldsymbol{\gamma}} + (1 - S)\int_{-\infty}^{t} \sum_{i=1}^{N} M_i(t - t')\boldsymbol{\gamma}_{[0]}(\boldsymbol{x}, t, t')\,\mathrm{d}t', \tag{11}$$

reduces to the convected Maxwell model when the solvent fraction S is zero, $S = 0$, and the memory function $M_i(t - t')$ is given by

$$M_i(t - t') = \frac{\eta_i}{\lambda_i^2}\exp(-(t - t')/\lambda_i). \tag{12}$$

Equation (11) gives the non-Newtonian stress of the fluid particle at position $\boldsymbol{x}$ at time t in terms of an integral over the deformation of that same particle at previous times t'. The tensor $\boldsymbol{\gamma}_{[0]}$ is the finite relative strain, related to the Finger strain tensor $\boldsymbol{B}$ by (Bird, Armstrong & Hassager 1987*a*)

$$\gamma_{[0]} = \boldsymbol{I} - \boldsymbol{B}. \tag{13}$$

When the parameter S, which is sometimes written as the ratio of a retardation time and a relaxation time, is non-zero, (11) is an integral form of the Oldroyd-B or convected Jeffreys constitutive model. These models describe a fluid with constant viscosity and constant normal stress coefficients in steady shear flow, characteristics of the class of polymer solutions known as Boger fluids.

The second integral model of interest here is given by

$$\boldsymbol{\tau}^p = -\mu\dot{\boldsymbol{\gamma}} + \int_{-\infty}^{t} \sum_{i=1}^{N} M_i(t - t')\frac{1}{1 - (1/\alpha)\,\mathrm{tr}(\boldsymbol{\gamma}_{[0]})}\boldsymbol{\gamma}_{[0]}(\boldsymbol{x}, t, t')\,\mathrm{d}t'. \tag{14}$$

Equation (14) is a simplified version of the model of Papanastasiou, Scriven & Macosko (1983), referred to hereafter as the PSM model. In the limit $\alpha \to \infty$, it has the same form as the convected Maxwell model. However, for finite α, it exhibits shear thinning both in the viscous and normal stress coefficients, and it therefore captures qualitative features that are exhibited by most polymeric liquids, but which are missing in (11). For a quantitative description of most viscoelastic fluids, one would require values of N equal to at least 3 or 4 (see, e.g., Barakos & Mitsoulis 1995). However, for purposes of comparison with other numerical results, it is convenient to choose $N = 1$. With this choice, the coefficient η_1 is the zero-shear viscosity η_0, $\eta_1 = \eta_0$, and λ_1 is the single relaxation time λ, $\lambda_1 = \lambda$. This simplification is made in all of the calculations described below.

3. Method of solution

As has been shown by others (Zheng *et al.* 1990; Pozrikidis 1992; Ladyzhenskaya 1969), the solution to (8) and (9) at a point $\boldsymbol{x}$ in the fluid can be expressed in integral form:

$$\boldsymbol{v}(\boldsymbol{x},t)=\boldsymbol{v}^{\infty}(\boldsymbol{x},t)-\frac{1}{4\pi\mu}\int_S \boldsymbol{J}(\boldsymbol{x},\boldsymbol{x}')\cdot[\boldsymbol{\sigma}(\boldsymbol{x}',t)\cdot\boldsymbol{n}(\boldsymbol{x}')]\,\mathrm{d}x'+\frac{1}{4\pi\mu}\int_A \boldsymbol{\tau}^p(\boldsymbol{x}',t):\nabla\boldsymbol{J}(\boldsymbol{x},\boldsymbol{x}')\,\mathrm{d}A. \tag{15}$$

Here positions within the flow are denoted by $\boldsymbol{x}$, and the first integral on the right-hand side of (15) is over the surface $\boldsymbol{S}$ bounding the flow. Like the imposed Newtonian velocity $\boldsymbol{v}^{\infty}$, the first integral contributes a Newtonian velocity field which, when combined with the non-Newtonian contribution from the integral of $\boldsymbol{\tau}^p$ over the flow domain A, satisfies the governing equations and no-slip boundary conditions. Note that the non-Newtonian stress $\boldsymbol{\tau}^p$ propagates a velocity disturbance as determined by the dipole propagator $\nabla\boldsymbol{J}$, as discussed above.

In a singularity method, the first two Newtonian terms on the right-hand side of (15) are replaced by a velocity field that is generated by summing contributions from singularities outside of the domain A. Here we use as these 'image singularities' N_{im} point forces with strength $\boldsymbol{F}^{im}$ and an equal number of point dipoles with strength $\boldsymbol{D}^{im}$, yielding

$$\boldsymbol{v}(\boldsymbol{x},t)=\frac{1}{4\pi\mu}\sum_{i=1}^{N_{im}}\left[\boldsymbol{J}(\boldsymbol{x},\boldsymbol{x}')\cdot\boldsymbol{F}_i^{im}+\boldsymbol{D}_i^{im}:\nabla\boldsymbol{J}(\boldsymbol{x},\boldsymbol{x}')\right]+\frac{1}{4\pi\mu}\int_A \boldsymbol{\tau}^p(\boldsymbol{x}',t):\nabla\,\boldsymbol{J}(\boldsymbol{x},\boldsymbol{x}')\,\mathrm{d}A. \tag{16}$$

In two dimensions, and for symmetric and traceless dipoles, $\boldsymbol{F}^{im}$ and $\boldsymbol{D}^{im}$ represent two unknowns each, which are chosen to impose the correct boundary conditions. In previous applications of this approach (Dabros 1985; Nitsche & Brenner 1990; Clague & Phillips 1996, 1997), a number of surface points N_s was chosen such that $N_s > 2N_{im}$, and the $2N_{im}$ unknowns were found by minimizing the deviation from no-slip conditions on S. Here we use a similar approach, but set $N_s = 2N_{im}$, so that the unknowns $\boldsymbol{F}^{im}$ and $\boldsymbol{D}^{im}$ are found by solving a linear system of equations, rather than by minimizing an error.

Since $\boldsymbol{\tau}^p$ is given by an integral equation that must be applied in a Lagrangian reference frame, it is convenient to rewrite (16) in such a frame. Let $\boldsymbol{x}(\alpha,t)$ be the trajectory of a fluid particle initially at position α. Then we have

$$\frac{\mathrm{d}\boldsymbol{x}}{\mathrm{d}t}(\alpha,t)=\boldsymbol{v}(\boldsymbol{x}(\alpha,t),t) \tag{17}$$

and

$$\boldsymbol{x}(\alpha,0)=\alpha, \tag{18}$$

with $\boldsymbol{v}$ given by (16). To transform the area integral in (16), we change variables of integration to Lagrangian coordinates (Anderson & Greengard 1985):

$$\int_A \boldsymbol{\tau}^p(\boldsymbol{x}',t):\nabla\boldsymbol{J}(\boldsymbol{x},\boldsymbol{x}')\,\mathrm{d}A=\int_{A^{\alpha}} \boldsymbol{\tau}^p(\boldsymbol{x}(\alpha',t),t):\nabla\boldsymbol{J}(\boldsymbol{x}(\alpha,t),\boldsymbol{x}(\alpha',t))\,\mathrm{d}^2\alpha'. \tag{19}$$

Here it has been used that, for an incompressible flow, the Jacobian of this transformation is unity (Chorin & Marsden 1993). The term $\mathrm{d}^2\alpha'$ in (19) indicates an integral over all the fluid particles in this two-dimensional problem.

The integration on the right-hand side of (19) is over the Lagrangian coordinate α, which for any fluid element is given by its position at time $t = 0$, as stated in (18). In other words, the integral is over the fluid particles, rather than over positions in space. To evaluate the integral numerically, we identify N_d dipole positions initially, where these positions are chosen in accordance with a quadrature scheme, such as a two-dimensional application of Simpson's rule, or a Gaussian quadrature. The weighting factors associated with the ith position α_i never change in a simulation, because they are determined by the Lagrangian coordinate α. Physically this result is simply a manifestation of the fact that, in an incompressible flow, the area (or volume in three dimensions) of a fluid element does not change in time. When evaluated numerically, the discretized integral on the right-hand side of (19) takes the form of a sum, and (16) becomes

$$\boldsymbol{v}(\boldsymbol{x}, t) = \sum_{i=1}^{N_{im}} \left[\boldsymbol{J}(\boldsymbol{x}, \boldsymbol{x}_i) \cdot \boldsymbol{F}_i^{im} + \boldsymbol{D}_i^{im} : \nabla \boldsymbol{J}(\boldsymbol{x}, \boldsymbol{x}_i) \right] + \sum_{j=1}^{N_d} \boldsymbol{D}_j : \nabla \boldsymbol{J}(\boldsymbol{x}, \boldsymbol{x}_j), \tag{20}$$

where the discretization entails letting

$$\boldsymbol{\tau}_j^p(\boldsymbol{x}_j, t)\, \mathrm{d}^2\alpha' \rightarrow \boldsymbol{D}_j, \tag{21}$$

and $\boldsymbol{\tau}^p$ is the non-Newtonian stress located at the position $\boldsymbol{x}_j = \boldsymbol{x}(\alpha_j, t)$. Note that the dipoles $\boldsymbol{D}_j$ in the fluid are distinguished from the image dipoles located outside the flow by the lack of the superscript *im*.

Because the position $\boldsymbol{x}_j$ moves with the fluid velocity, one can apply directly constitutive equations that are written in Lagrangian coordinates, such as (11) and (14). To evaluate the integrals in those equations, one must calculate and store the Finger strain $\boldsymbol{B}(\boldsymbol{x}_j, t')$ at each position $\boldsymbol{x}_j$, relative to a series of reference times t'. To do this calculation, we use the fact that $\boldsymbol{B}$ can be related to a displacement gradient tensor $\boldsymbol{E}$ by

$$\boldsymbol{B} = \boldsymbol{E} \cdot \boldsymbol{E}^t, \tag{22}$$

and in a Lagrangian reference frame the tensor $\boldsymbol{E}$ for a given fluid element changes in time according to (Bird *et al.* 1987*a*)

$$\frac{\mathrm{d}\boldsymbol{E}}{\mathrm{d}t'} = -\boldsymbol{E} \cdot \nabla \boldsymbol{v}^t \tag{23}$$

with

$$\boldsymbol{E} = \boldsymbol{I} \quad \text{at} \quad t' = t. \tag{24}$$

Integration of (23) for the N_d fluid elements to find $\boldsymbol{E}(\boldsymbol{x}_j, t')$ for a series of times t', for each fluid particle, yields the required information.

A time step in a simulation is achieved as follows. By using (23), the displacement gradient tensor $\boldsymbol{E}$, and hence $\boldsymbol{B}$ and $\boldsymbol{\gamma}_{[0]}$ via (22) and (13), is incremented in time. Here these increments are chosen according to a fourth-order Runge–Kutta method. The new value of $\boldsymbol{\gamma}_{[0]}$ is used in (11) or (14) to update $\boldsymbol{\tau}^p$, leading to new values of the dipole strengths $\boldsymbol{D}$ through (21). With the new dipole strengths, (20) is written at $2N_{im}$ surface points, and no-slip conditions are imposed, yielding a linear set of equations for the unknown image singularities $\boldsymbol{F}^{im}$ and $\boldsymbol{D}^{im}$. Once these are known, the entire right-hand side of (20) can be evaluated, and the next step in the Runge–Kutta integration can begin.

Note that the matrix formed from the equations governing $\boldsymbol{F}^{im}$ and $\boldsymbol{D}^{im}$ depends only on the positions of the N_{im} singularities and $2N_{im}$ surface points, which do not

evolve in time. Hence, the LU decomposition of the matrix can be stored, and the solution of the linear equations requires computation time that scales as N_{im}^2. Since there are many more dipoles in the fluid than image singularities, $N_d \gg N_{im}$, the time requirement for each step is dominated by the need to update $\boldsymbol{B}$ at the N_d dipole positions. In the next subsection, we discuss a method for calculating these dipole–dipole interactions that avoids numerical instabilities that can arise due to the singular nature of the dipole propagator $\nabla \boldsymbol{J}$. Then, in § 3.2, a method for rapidly summing the dipole–dipole interactions is explained.

3.1. *Cutoff functions*

Because the dipole propagator $\nabla \boldsymbol{J}(\boldsymbol{x})$ is singular as $r \to 0$, it is evident that whenever two dipoles approach one another, the velocity disturbance from the resulting interaction becomes singular also. This same problem is present in the point vortex method for calculating inviscid flows, mentioned in the Introduction (Puckett 1993). Interestingly, in the point-vortex literature it has been shown that, for a smooth flow, an even distribution of points moving with a fluid remains evenly distributed (Goodman, Hu & Lowengrub 1990), so that the dipoles should remain well-separated if they are so initially. Nonetheless, in practice it is found that it is necessary to remove the singular nature of the interactions for the point-vortex method to yield good results, and we have found the same to be true for the point-dipole method. This 'desingularization' is achieved by using what are termed 'cutoff functions', which effectively distribute a singularity over a small region around its centre, changing a point vortex into a particle vortex or 'vortex blob'. We now derive cutoff functions for the point-dipole method by using an approach that is conceptually similar to that been used for the particle-vortex method.

The propagator $\nabla \boldsymbol{J}$, where $\boldsymbol{J}$ is as given in (7), may be written in the form (Pozrikidis 1992)

$$\nabla \boldsymbol{J}(\boldsymbol{x}) = \frac{1}{\mu} \nabla (\nabla\nabla - \boldsymbol{I}\nabla^2) H(r), \tag{25}$$

where $r = (\boldsymbol{x} \cdot \boldsymbol{x})^{1/2}$ and the function $H(r)$ is the solution to

$$\nabla^2 \nabla^2 H = \delta_s(\boldsymbol{x}). \tag{26}$$

One method of smoothing the dipole propagator $\nabla \boldsymbol{J}$ is to replace the Dirac delta $\delta_s(\boldsymbol{x})$ in (26) with a non-singular, numerical approximation to it, $f_\delta(\boldsymbol{x})$, which becomes identical to the Dirac delta in the limit where the cutoff parameter δ_c approaches zero, and which yields a value of unity when integrated over position $\boldsymbol{x}$.

We therefore define a function $H_\delta(r)$ as the solution to

$$\nabla^2 \nabla^2 H_\delta = f_\delta(\boldsymbol{x}), \tag{27}$$

and a desingularized propagator $\nabla \boldsymbol{J}_\delta$ by

$$\nabla \boldsymbol{J}_\delta(\boldsymbol{x}) = \frac{1}{\mu} \nabla (\nabla\nabla - \boldsymbol{I}\nabla^2) H_\delta(r). \tag{28}$$

For radially symmetric choices of $f_\delta(r)$, it can be shown that $\nabla \boldsymbol{J}_\delta$ is related to $\nabla \boldsymbol{J}$ by a function $F(r)$ according to

$$\nabla \boldsymbol{J}_\delta = \nabla \boldsymbol{J} F(r), \tag{29}$$

where the function $F(r)$ satisfies

$$\frac{\mathrm{d}F}{\mathrm{d}r} = f_\delta(r) 2\pi r \tag{30}$$

or

$$F(r) = \int_0^r f_\delta(s) 2\pi s \, \mathrm{d}s. \tag{31}$$

Interestingly, the results (29)–(31) are completely analogous to what is found for the particle-vortex method (Puckett 1993), even though the propagators (or kernels) are different. An example of deriving a cutoff function $F(r)$ by using a Gaussian approximation to the Dirac delta function is given below.

Physically, replacing the Dirac delta $\delta_s(\boldsymbol{x})$ in (26) with the approximate function $f_\delta(\boldsymbol{x})$ in (27) amounts to delocalizing, or spreading, the location of the singular dipole over a radially symmetric region with an area that is $O(\delta_c^2)$. This process is a recognition of the fact that the dipolar character of a fluid element is spread throughout the element, and its concentration to a point is only done for purposes of numerically evalutating the area integral in (16). Thus, in a sense the desingularization undoes the concentration of dipole strength at a point in space that is needed to proceed from (19) to (20). In the particle-vortex literature, the resulting entity is sometimes referred to as a vortex blob, and in the current context one could similarly speak of a dipolar or elastic blob.

The spreading out of the dipole strength inherent in using $\nabla \boldsymbol{J}_\delta$ in place of $\nabla \boldsymbol{J}$ in no way takes account of the presence of the boundaries. Boundaries could be taken into account if a function $f_\delta(\boldsymbol{x})$ were used that is not radially symmetric, but that complication is not explored here, nor does it appear to be necessary although it could reduce numerical error. Instead, to avoid the aphysical act of spreading a dipole through the surface S, the original propagator $\nabla \boldsymbol{J}$ is used to calculate dipole contributions to the velocity on S. In addition, since the image singularities are not in the fluid, and their positions are fixed, their velocity disturbances are also calculated with the original propagators, which are $\boldsymbol{J}$ and $\nabla \boldsymbol{J}$ for $\boldsymbol{F}^{im}$ and $\boldsymbol{D}^{im}$, respectively.

To derive the cutoff function used in our calculations, a Gaussian form for the function $f_\delta(\boldsymbol{x})$ is used,

$$f_\delta(\boldsymbol{x}) = \frac{1}{\pi \delta_c^2} \exp\left(-r^2/\delta_c^2\right), \tag{32}$$

which clearly yields unity upon integration, $\int f_\delta 2\pi r \, \mathrm{d}r = 1$. Substituting into (31) yields

$$F_2(r) = 1 - \exp\left(-r^2/\delta_c^2\right), \tag{33}$$

and $\nabla \boldsymbol{J}_\delta$ follows trivially from (29). As $r \to 0$, the smoothed propagator $\nabla \boldsymbol{J}_\delta \to 0$, but for $r \gg \delta_c$ it is evident that $\nabla \boldsymbol{J}_\delta = \nabla \boldsymbol{J}$. The cutoff function $\boldsymbol{F}_2(r)$ is used to calculate all of the results presented in the next section.

To evaluate the usefulness of other possible cutoff functions, and to identify plausible choices for the cutoff parameter δ_c, it is helpful to consider the error incurred by substituting $\nabla \boldsymbol{J}_\delta$ for $\nabla \boldsymbol{J}$ in (19). To this end, we define a function $g(\boldsymbol{x}, t) - \boldsymbol{g}_\delta(\boldsymbol{x}, t)$ as

$$\boldsymbol{g}(\boldsymbol{x}, t) - \boldsymbol{g}_\delta(\boldsymbol{x}, t) = \int_A \boldsymbol{\tau}^p(\boldsymbol{x}(\alpha', t), t) : \nabla \boldsymbol{J}(\boldsymbol{x}(\alpha, t), \boldsymbol{x}(\alpha', t)) \, \mathrm{d}\alpha - \sum_{j=1}^{N_d} h_j \boldsymbol{D}_j : \nabla \boldsymbol{J}_\delta(\boldsymbol{x}, \boldsymbol{x}_j) \tag{34}$$

and seek the magnitude of the difference, $|\boldsymbol{g}(\boldsymbol{x}, t) - \boldsymbol{g}_\delta(\boldsymbol{x}, t)|$. Following Anderson & Greengard (1985), we separate the desired quantity into two error terms, e_m and e_d,

where

$$e_m = \int_A \boldsymbol{\tau}^p(\boldsymbol{x}(\alpha', t), t) : \nabla \boldsymbol{J}(\boldsymbol{x}(\alpha, t), x(\alpha', t))\, \mathrm{d}\alpha - \int_A \boldsymbol{\tau}^p(\boldsymbol{x}(\alpha', t), t) : \nabla \boldsymbol{J}_\delta(\boldsymbol{x}(\alpha, t), \boldsymbol{x}(\alpha', t))\, \mathrm{d}\alpha, \tag{35}$$

and

$$e_d = \int_A \boldsymbol{\tau}^p(\boldsymbol{x}(\alpha', t), t) : \nabla \boldsymbol{J}_\delta(\boldsymbol{x}(\alpha, t), \boldsymbol{x}(\alpha', t))\, \mathrm{d}\alpha - \sum_{j=1}^{N_d} h_j \boldsymbol{D}_j : \nabla \boldsymbol{J}(x, x_j). \tag{36}$$

Clearly $|\boldsymbol{g}(\boldsymbol{x}, t) - \boldsymbol{g}_\delta(\boldsymbol{x}, t)| = e_m + e_d$, where e_m accounts for errors from replacing $\nabla \boldsymbol{J}$ with $\nabla \boldsymbol{J}_\delta$, and e_d for errors from evaluating the integral over $\nabla \boldsymbol{J}_\delta$ numerically.

Although the kernel $\nabla \boldsymbol{J}$ is more complicated than that used for the point-vortex method, it is mathematically similar to it in that it is odd with respect to position $\boldsymbol{x}$, and decays as $1/r$, i.e.

$$\frac{\partial J_{ij}}{\partial x_k} = \frac{1}{4\pi\mu r^2}\left(-\delta_{ij}x_k + \delta_{ik}x_j + \delta_{jk}x_i - \frac{2x_i x_j x_k}{r^2}\right). \tag{37}$$

Indeed, the developments used by Anderson & Greengard (1985) for the point-vortex method apply to the current problem with little modification. We restrict the analysis to functions $f_\delta(\boldsymbol{x})$ that are L times continuously differentiable, where x is position in two dimensions, and which satisfy

$$\int f_\delta(\boldsymbol{x})\, \mathrm{d}\boldsymbol{x} = 1 \tag{38}$$

and

$$\int \boldsymbol{x}^\beta f_\delta(\boldsymbol{x})\, \mathrm{d}\boldsymbol{x} = 0 \quad \text{for all} \quad 1 \leqslant |\beta| \leqslant m - 1. \tag{39}$$

(For further conditions on the boundedness and differentiability of f_δ, see Anderson & Greengard 1985 or Puckett 1993.) Then the errors e_m and e_d satisfy

$$e_m \leqslant C_m \delta_c^m \quad \text{and} \quad e_d \leqslant C_d(\Delta/\delta_c)^L \delta_c, \tag{40}$$

where m is identified through (39), and is referred to as the order of the cutoff function. The function $f_\delta(\boldsymbol{x})$ in (32), like any radially symmetric function satisfying (38), is a second-order cutoff function (i.e. $m = 2$), and hence the subscript 2 on $F_2(r)$ in (33).

The result for e_m in (40) quantifies the otherwise expected result that using the approximate kernel $\nabla \boldsymbol{J}_\delta$ is more accurate for smaller values of δ_c, with an error of $O(\delta_c^2)$ for the cutoff function given in (33). The result for e_d in (40) was obtained by assuming the discretization of the area integral to be consistent with the trapezoid rule, with points separated by a distance Δ on a rectangular grid. For the Gaussian function in (32), the differentiability L can be considered arbitrarily high. It is therefore apparent that the cutoff parameter δ_c must be larger than the point-to-point spacing Δ, $\delta_c > \Delta$, which implies that the cores of the dipolar blobs must overlap. In practice, in particle-vortex calculations researchers have often let $\delta_c = h^p$, with the parameter p in the range $1/2 < p < 1$. The results for the point-dipole method are similar, in that a value of p of approximately 0.75 seems to yield good results. In addition, it is necessary to have δ_c larger than the average dipole–dipole spacing to be able to

achieve a steady state in the journal-bearing flows examined here, even at very low Weissenberg numbers.

It is of interest to compare these errors with estimates for more conventional approaches, such as the Galerkin finite element method. For a triangular mesh with three nodes per element (i.e. linear triangular elements), the error is $O(h)$, where h is the length of a side of an element. If quadratic triangular elements are used, with six nodes per element, then the error is $O(h^2)$ (Chung 1978). These errors and the estimates in (40) therefore scale comparably with the number of unknowns. However, we note that the estimates for e_d and e_m in (40) do not take account of errors associated with imposing the no slip boundary conditions. As discussed in § 4 below, using isotropic cutoff functions near boundaries can introduce errors of $O(\delta_c)$ into the point-dipole method. Hence the estimates in (40) provide a useful guide for choosing cutoff functions and related parameters such as δ_c, but further work is needed on methods for smoothing dipole–dipole interactions near boundaries.

In addition to the Gaussian function given in (32), we also performed some trial calculations with the function

$$f_\delta(\boldsymbol{x}) = \frac{1}{\pi\delta_c^2}\left[2\exp\left(-r^2/\delta_c^2\right) - \tfrac{1}{2}\exp\left(-r^2/2\delta_c^2\right)\right], \tag{41}$$

which yields the fourth-order cutoff function

$$F_4(r) = 1 - 2\exp\left(-r^2/\delta_c^2\right) + \exp\left(-r^2/2\delta_c^2\right). \tag{42}$$

In spite of the fact that the error associated with (42) is smaller than that with (32), computations with it did not show significant improvement over (33). In addition, (42) decays more slowly than the second-order cutoff in (32), and requires more computation time to compute, and for those reasons it was decided to use the second-order result $F_2(r)$. Although there are other cutoff functions that are of high order and avoid the computationally expensive exponential term (see e.g. Puckett 1993), those have not yet been used in our simulations.

3.2. *Fast multipole method*

Evaluation of the right-hand side of (20) requires that one evaluate both the velocity and the velocity gradient at the position of each dipole. Since each dipole interacts with every other dipole, calculating these quantities in a straightforward way requires $O(N_d^2)$ operations, and is not feasible for many problems. However, it has been shown previously (Greengard 1988; Greengard & Rokhlin 1997) that interactions between multipoles need not be calculated individually when they are sufficiently far apart. For distant dipoles, groupings or cells can be created, and their interactions used in place of interactions between individual dipoles. As the distance between cells grows larger, the cell size is increased, resulting in a method that is $O(N_d)$, rather than $O(N_d^2)$.

A schematic diagram of how such a method can be implemented for the current problem is shown in figure 2. The annular region of flow is divided into a hierarchy of approximately square cells, where in this case the largest cells have a dimension of approximately one-third of the gap size. Each large cell consists of four intermediate cells, which in turn consist of four small cells. More divisions could be created, but these were sufficient for the current problem. In figure 2 the interaction between Cells M and N is shown, because they are so far apart relative to the spacing between dipoles within each individual cell that using groups rather than individual dipoles introduces no significant error into the calculation.

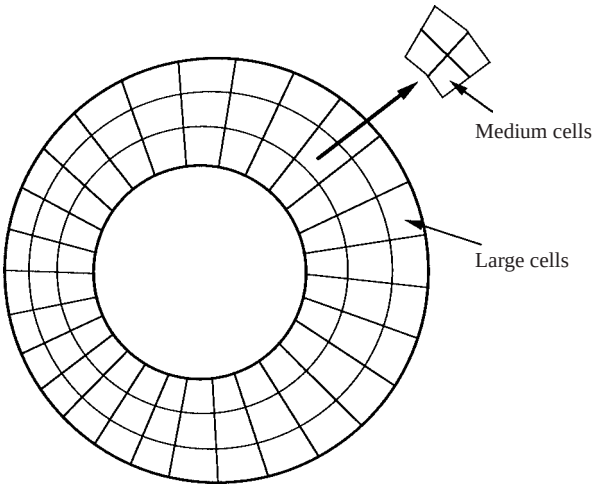

FIGURE 2. Diagram of large and medium cells used to implement the fast multipole method for summing multipole interactions. Each medium cell contains four small cells that are not shown.

To calculate interactions, one first computes the sum of all the dipole strengths in each cell, and places the resulting 'super dipole' at the average dipole position in each cell. As a first approximation, the contribution of the dipoles in Cell N to the velocity at the positions of the dipoles in Cell M can be found by calculating the velocity disturbance of the super dipole at Cell N at the position of Cell M. To improve upon this estimate, one must account for the fact that the dipoles in Cells M and N are displaced slightly (relative to the cell–cell separation) from the cell centres. This refinement is done by improving the multipole representation of Cell N (i.e. including the quadrupole term), and by creating a Taylor expansion of the velocity disturbance from Cell N about the centre of Cell M.

The strengths $\boldsymbol{D}_N^{SD}$ and positions $\boldsymbol{x}_N^c$ of the super dipoles in the Nth cell are given by

$$\boldsymbol{x}_N^c = \frac{1}{N_{c,N}} \sum_j \boldsymbol{x}_{N,j} \tag{43}$$

and

$$\boldsymbol{D}_N^{SD} = \sum_j \boldsymbol{D}_{N,j}, \tag{44}$$

where $N_{c,N}$ is the number of dipoles, $\boldsymbol{x}_{N,j}$ is the position of the jth dipole, and $\boldsymbol{D}_{N,j}$ the strength of the jth dipole in the Nth cell. The velocity disturbance $\boldsymbol{v}'_{M,N}$ of the Nth cell at the position of the Mth cell is then

$$\boldsymbol{v}'_{M,N} = \boldsymbol{D}_N^{SD} : \nabla \boldsymbol{J}(\boldsymbol{x}_M - \boldsymbol{x}_N). \tag{45}$$

The strategy for calculating multipoles such as $\boldsymbol{D}_M^{SD}$ for all the cells is discussed below. Note also that the propagator $\nabla \boldsymbol{J}$ decays as $1/r$, and hence the approximation given by (45) must be improved (by including higher-order multipoles) unless the separation between the cells is hundreds of times larger than the cell dimensions.

The improvement is obtained by accounting for variations in the dipole positions about the centre of Cells M and N, a factor which is neglected in the first approximation in (45). To account for variations in the dipole positions about the

centre of Cell N, we use the quadrupole moment $\boldsymbol{Q}_N$ of that cell:

$$\boldsymbol{Q}_N = \sum_j (\boldsymbol{x}_j - \boldsymbol{x}_N)\boldsymbol{D}_{N,j}. \tag{46}$$

The quadrupole $\boldsymbol{Q}_N$ creates an adjustment $\Delta\boldsymbol{v}'$ to the velocity disturbance given in (45), where

$$\Delta v'_w = -Q_{N,rks}\frac{\partial}{\partial x_r}\frac{\partial}{\partial x_k}\boldsymbol{J}_{sw}(\boldsymbol{x}_M - \boldsymbol{x}_N). \tag{47}$$

In (47), indicial notation has been used to clarify the nature of the triple dot product between the quadrupole $\boldsymbol{Q}_N$ and the propagator $\nabla\nabla\boldsymbol{J}$. The subscript M, N has been omitted on the left-hand side, to avoid confusion between the various indices, it being understood that the result in (47) is to be added to that in (45). The negative sign is present because the extra gradient is with respect to $\boldsymbol{x}_N$.

To complete the calculation of terms that decay as $1/r^2$, the effect of the varying positions of the dipoles in the Mth cell must also be taken into account. This term is found by recognizing $\boldsymbol{v}'_{M,N}$ in (45) as the first term of a Taylor expansion about the cell centre $\boldsymbol{x}_M$, and calculating the $1/r^2$ correction $\Delta\boldsymbol{v}''_j$ for the velocity at the position of the jth dipole:

$$\Delta\boldsymbol{v}''_j = (\boldsymbol{x}_j - \boldsymbol{x}_M)\cdot\nabla_M\boldsymbol{v}'_{M,N}. \tag{48}$$

The subscript M on ∇_M indicates that the derivative is with respect to $\boldsymbol{x}_M$. Interactions other than those in (45), (47) and (48) decay as $1/r^3$ or faster, and are neglected here.

Implementation of the fast multipole method requires calculation of the super dipoles in (45) and the quadrupoles in (47) for the small, intermediate and large cells shown in figure 2. This calculation is best performed by starting with the small cells, for which $\boldsymbol{D}^{SD}$ and $\boldsymbol{Q}$ can be calculated in $O(N_d)$ operations. Once these are obtained, the corresponding quantities for the intermediate and large cells follow in a straightforward fashion. Clearly the super dipole for an intermediate cell is simply the sum of those of its four constituent small cells, and its position is the average position of the constituent cells. Similarly, the positions and super dipoles of the large cells can be computed from those of the intermediate cells. Calculation of the quadrupoles for the intermediate cells from those of the small cells requires that the centre about which $\boldsymbol{Q}$ is calculated be shifted. In terms of Cartesian vectors and tensors, this shifting of positions is relatively simple. If $\boldsymbol{x}_M$ is the centre of an intermediate cell, and $\boldsymbol{x}_m$ that of one of its four constituent small cells, then the contribution of the quadrupole $\boldsymbol{Q}_m$ of the small cell to the quadrupole $\boldsymbol{Q}_M$ of the intermediate cell is

$$\boldsymbol{Q}'_M = \sum_j (\boldsymbol{x}_j - \boldsymbol{x}_M)\boldsymbol{D}_{M,j} = \boldsymbol{Q}_m + (\boldsymbol{x}_m - \boldsymbol{x}_M)\boldsymbol{D}^{SD}_m. \tag{49}$$

In (49), the superscript prime on $\boldsymbol{Q}'_M$ indicates that the right-hand side is the contribution of one of the constituent cells to the quadrupole $\boldsymbol{Q}_M$; to complete the calculation of $\boldsymbol{Q}_M$, the other three small cells would also have to be included. Clearly if the quadrupoles $\boldsymbol{Q}_m$ and super dipoles $\boldsymbol{D}^{SD}_m$ of the small cells are known, they can be used to calculate the quadrupoles of the intermediate cells; the quadrupoles for the large cells are obtained in an analogous fashion.

Calculation of dipole–dipole interactions by using cells as described above involves neglecting interactions that are $O(r_c/r)^3$, where r_c is the dimension of the cell and r the cell–cell separation. In the implementation used here, interactions between dipoles closer than 20 times the size of the smallest cell are calculated individually; dipoles

FIGURE 3. Schematic diagram of the dipole regeneration method used to make simulations stable for an indefinite period of time.

farther than 20 times the smallest cell size, but closer than 20 times the size of the intermediate cells (which are themselves double the size of the small cells) are calculated by using the small cells; dipoles farther than 20 times the intermediate cell size, but closer than 20 times the size of the large cells are calculated by using the intermediate cells; and dipoles farther than 20 times the large cell size are calculated by using the large cells. By using this conservative approach, it is ensured that negligible error is introduced with the fast multipole method.

Although the FORTRAN code used here is far from being fully optimized, using the fast multipole method increased the computational speed by orders of magnitude. For a simulation with 120 000 dipoles, a single time step (requiring four full calculations for the Runge–Kutta integration) used 2 hours of CPU time on a one-processor, 600 MHz, Pentium III computer. Approximately 300 MB of RAM were typically required, with the maximum allowed by the Pentium processors being 512 MB. Because the need for processor time is dominated by the calculation of dipole–dipole interactions, including more relaxation times in the memory functions $M(t-t')$ in (11) and (14) would have a negligible impact on the computation time per step. Shorter relaxation times would require smaller time steps, but the same is true for resolving the time derivatives in differential constitutive models. Including additional relaxation times λ_i that are small compared to the inverse of the rate of deformation, $\lambda_i \ll 1/\dot{\gamma}$, could be facilitated by approximating the strain terms in (11) and (14) as constant, or by using Taylor expansions in $(t-t')/\lambda_i$, thereby allowing analytic evaluation of the integrals.

3.3. *Regeneration of dipoles*

In the method described above, a single population of dipoles is introduced at the start of a simulation, and their trajectories are calculated by direct integration of the velocity. Although this approach is adequate for many calculations, at long enough times it is likely that small errors in the velocity will accumulate to the point where they distort the distribution of dipoles. To avoid this problem, it is necessary to limit the lifetime of any one population of dipoles, thereby limiting the effect of small errors in the velocity.

To achieve this goal, one can periodically create and destroy a fraction of the dipoles in a simulation, as shown schematically in figure 3. The three populations of dipoles are denoted Population 1, Population 2 and Population 3, and they account for periods of the time integration of $t-\tau_1 < t' < t$, $t-\tau_2 < t' < t-\tau_1$ and $t-T < t' < t-\tau_2$, respectively. The total time of integration is therefore from $t' = t-T$ to $t' = t$, where T is taken to be 7.2λ. The times τ_1 and τ_2 are ordered such that $\tau_2 > \tau_1$.

When Population 1 is first created, $\tau_1 = 0$ and $\tau_2 = T/2$, so that Populations 2 and 3 account for the entire integral over t'. At each time step, τ_1 and τ_2 are increased, until $\tau_1 = T/2$ and $\tau_2 = T$. At this point, Population 3 is destroyed, Populations 1 and 2 are promoted to become Populations 2 and 3, respectively, and a new Population 1 is created, always at the locations specified by the two-dimensional integration method being employed. In this way, no dipole ever exists for a time longer than T,

regardless of how long a simulation continues. Unfortunately, the number of dipoles required is three times larger than would otherwise be the case, but in many instances the stability for arbitrarily long times is worth this cost. Obviously, more than three populations could be used, but this would increase the number of required dipoles still further. In § 4 below, the number of dipoles quoted is always the number in one population.

4. Results and discussion

To evaluate the accuracy, stability and feasibility of the method described above, we have calculated non-Newtonian flows in a journal bearing as shown in figure 1, and also in a wide-gap concentric cylinder geometry. In the limit where the gap is small, $\delta \ll 1$, there is a lubrication flow in the journal bearing in which high pressure builds at the entrance to the thin-gap region (i.e. where $x < 0$ and $y > 0$), and low pressure develops at the exit to that region. For a Newtonian flow at low Reynolds number, the result is a large force in the $-\boldsymbol{e}_y$-direction acting on the inner cylinder, but no force in the $\boldsymbol{e}_x$-direction. For viscoelastic flows, normal stresses act on the inner cylinder over its whole perimeter, $0 < \theta < 2\pi$. However, they are stronger in the thinner gap on the left-hand side where $x < 0$, resulting in a net force in the $+\boldsymbol{e}_x$-direction. Since this effect is a result of a competition between nearly equal stresses acting over the inner cylinder, it is quite sensitive to error in any region of the annulus, and the dimensionless force $F_x/\mu\Omega R_0$ is therefore a useful parameter for tracking these non-Newtonian flows.

Before proceeding we note that elastic instabilities are known to occur in these flows, both for the concentric and eccentric cylinder geometries (Larson, Muller & Shaqfeh 1990; Larson, Muller & Shaqfeh 1994; Chawda & Avgousti 1996; Dris & Shaqfeh 1998). However, these instabilities occur at Weissenberg numbers at least an order of magnitude greater than those used in the simulations described here, which always pertain to values less than unity, $Wi < 1$. Two-phase flows, such as are described in § 4.3, also exhibit elastic instabilities (Grillet, Lee & Shaqfeh 1999), at lower Weissenberg numbers than the one-phase systems, but still only for values greater than unity, $Wi > 1$. In addition, these two-phase 'ribbing' instabilities have been observed for systems partially filled with liquid and partially with air, undergoing a steady rotation. Those conditions differ significantly from those considered here, in which there are two liquids with equal densities and steady-shear viscosities, being subjected to a slow oscillatory rotation. All the results reported in this section were therefore obtained at conditions that should be free from the effects of elastic instabilities.

4.1. *Normal stresses in the journal bearing*

In the limit of low elasticity, $Wi \to 0$, the convected Maxwell model given by (11) and (12) with $S = 0$ simplifies to a form of the second-order fluid (SOF) constitutive model. For the SOF model, an exact solution to flow in a journal bearing has been derived by Ballal & Rivlin (1976). Their results, calculated from equation (51) of their paper, and results from the PDM are shown in table 1 for a gap size $\mu = 0.11$ and an eccentricity ε in the range $0 < \varepsilon < 0.4$. The results for the PDM were calculated at $Wi = 0.05$ and $N_d = 41\,353$, and agree with the exact result to within 4%. We note again that the force in the x-direction is not simply the force exerted by normal stresses, but is the result of a slight imbalance between the normal stresses in the thin- and wide-gap regions of the flow. Obtaining good agreement from a numerical

ε	Ballal & Rivlin (1976)			Point-dipole method		
	$\dfrac{F_x}{\eta_0 \Omega R_i De}$	$\dfrac{F_y}{\eta_0 \Omega R_i}$	$\dfrac{L_z}{\eta_0 \Omega R_i^2}$	$\dfrac{F_x}{\eta_0 \Omega R_i De}$	$\dfrac{F_y}{\eta_0 \Omega R_i}$	$\dfrac{L_z}{\eta_0 \Omega R_i^2}$
0.1	101.9	160.8	67.1	105.6	163.3	67.5
0.2	206.9	321.9	70.6	214.9	326.7	70.9
0.3	319.9	484.1	76.4	332.4	491.3	76.8
0.4	450.2	649.9	84.9	470.3	659.9	85.4

TABLE 1. Comparison at low *De* with exact solution for second-order fluids.

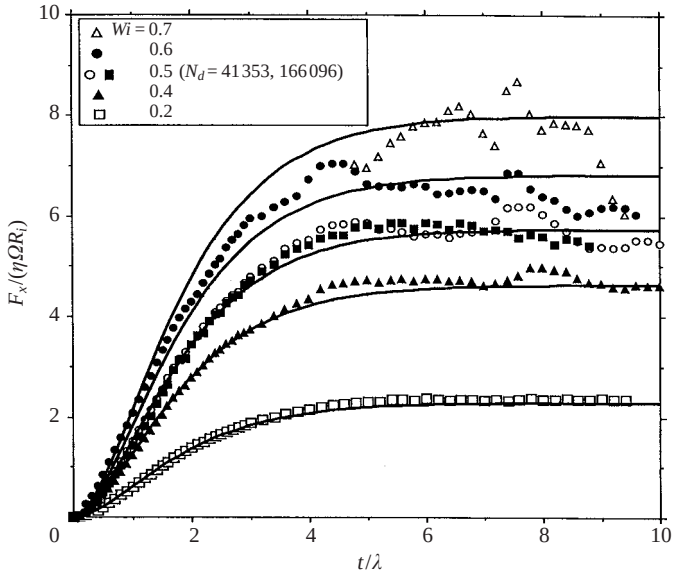

FIGURE 4. Simulation results for the x-directed force on the inner cylinder obtained with the convected Maxwell constitutive model, for Weissenberg numbers in the range $0 < Wi \leqslant 0.7$. Solid curves are computed from (50) multiplied by the expected time dependence $1 - (1 + t/\lambda)\mathrm{e}^{-t/\lambda}$.

calculation of this imbalance, even at eccentricities as low as $\varepsilon = 0.1$, shows that the point–dipole method yields very accurate forces in weakly elastic flows.

Time-dependent results for $F_x/\eta_0 \Omega R_0$ at higher Weissenberg numbers, $0 < Wi < 0.7$, are shown in figure 4, again for the convected Maxwell model. Here the eccentricity is $\varepsilon = 0.1$, the gap is again $\delta = 0.11$, and the inner cylinder has been started abruptly from rest. In the limit where the gap is small, $\delta \ll 1$, the eccentricity is small, $\varepsilon \ll 1$, and the Deborah number (but not necessarily Wi) is small, $De \ll 1$, the flow in the journal bearing is approximately viscometric in nature. Under such conditions, most constitutive equations reduce to a common form, known as the Criminale–Ericksen–Filbey (CEF) equation, for arbitrary values of the Weissenberg number Wi. Phan-Thien & Tanner (1981) used the CEF equation to derive the following result for the x-directed force:

$$\frac{F_x}{\eta_0 \Omega R_0} = \frac{4\pi\varepsilon}{\delta} Wi. \tag{50}$$

The force in (50) is a direct result of the first normal stress difference in the fluid. For a Maxwell fluid, this normal stress difference grows in time according to the function $1-(1+t/\lambda)\mathrm{e}^{-t/\lambda}$ following start-up of a steady viscometric flow (Bird *et al.* 1987). The solid curves shown for comparison in figure 4 are, therefore, this function of time multiplied by $F_x/\eta_0\Omega R_0$ from (50). Both the final steady x-directed force and the predicted time-dependent rate of growth are in good agreement with the computed results.

The results shown in figure 4 were obtained with 41 353 dipoles, with the exception of one simulation at $Wi = 0.5$, where the number of dipoles was approximately quadrupled (the dipole spacing was reduced by half) to 166 096. Up to $Wi = 0.5$, stable and accurate results are obtained. The simulation with $N_d = 166\,096$ confirms that the results are converged with respect to the number of dipoles, since the two sets of results at $Wi = 0.5$ are in very good agreement. Although the higher number of dipoles smooths the behaviour in time, it is virtually certain that eventually a simulation that always makes use of the same population of dipoles will become inaccurate, whereas periodically introducing new populations should make the simulation stable indefinitely. This matter is of some importance in, for example, simulations of suspensions of particles or drops, where the simulation time may need to be hundreds of relaxation times long.

At $Wi = 0.6$, a steady result is still obtained with $N_d = 41\,353$, but the calculated force shows greater fluctuations in time, with deviations up to 10% from the predicted steady force being apparent. At $Wi = 0.7$, the simulation reaches a fluctuating result approximately equal to the expected value (cf. (50)) for $6\lambda < t < 9\lambda$, but becomes unstable at approximately $t = 9\lambda$. The time step used in the fourth-order Runge–Kutta integration was $\Delta t = 0.1\lambda$ at the lower Weissenberg numbers $Wi < 0.6$, and $\Delta t = 0.05\lambda$ for $Wi = 0.6$ and 0.7. The two time steps gave identical results at $Wi = 0.5$, but showed a slight difference at $Wi = 0.6$, which is why the smaller time step was used at the faster rotation rates.

A fluctuation is visible for the larger Weissenberg numbers, $Wi > 0.4$, at the time $t = 7.2\lambda$ when a new population of dipoles (i.e. Population 3) is introduced. That this is the cause of the fluctuation is confirmed by the fact that the fluctuation is missing in the simulation with $N_d = 166\,096$, in which only one population of dipoles was used. The conversion from integrating over Eulerian positions in space to an integration over material or Lagrangian position, as described in (16) and (19), presupposes a velocity field that exactly satisfies conservation of mass. However, as noted above, the velocity calculated with the smoothed propagator $\nabla \boldsymbol{J}_\delta$ does not satisfy the continuity equation exactly as long as δ_c is finite. As the dipole positions are advanced with the fluid velocity, deviations from purely incompressible flow lead to inaccuracies in the area integral, and fluctuations appear when new populations of dipoles, not yet affected by the fluid velocity, are introduced. The presence of small fluctuations of this type can be tolerated. To eliminate them, one must either improve the accuracy of the velocity field, or use more dipole populations that are introduced more frequently. Either option, of course, comes at the cost of increased computation time.

In figure 5, results are shown that are comparable to those in figure 4, but for an Oldroyd-B fluid with a solvent fraction $S = 0.85$. As was found by Rajagopalan *et al.* (1993), relative to the convected Maxwell model, this model is more stable because of the purely viscous solvent contribution, and results were obtained in the range $0 < Wi < 0.9$. All of these results were obtained at $N_d = 41\,353$, and dipole regeneration was used in all cases. At $Wi = 0.6$, the time step $\Delta t = 0.1\lambda$ yielded results identical to those obtained at $\Delta t = 0.05\lambda$, as shown. However, small differences

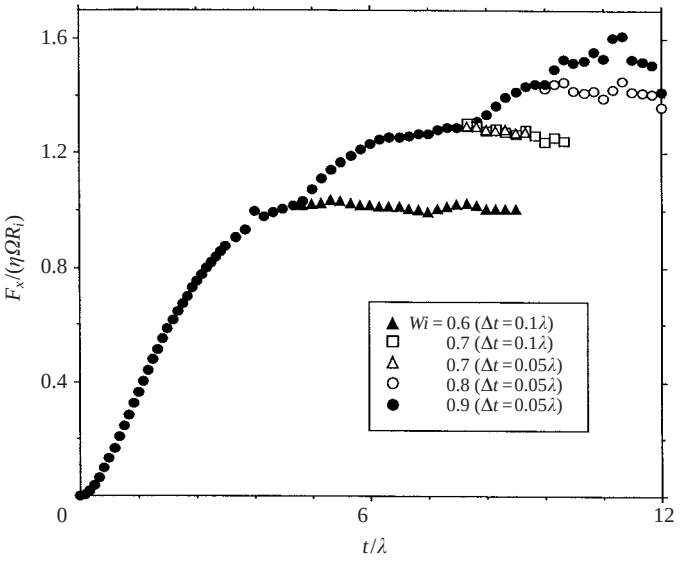

FIGURE 5. Simulation results for the x-directed force on the inner cylinder obtained with the Oldroyd-B constitutive model with $S = 0.85$, for Weissenberg numbers in the range $0.6 \leqslant Wi \leqslant 0.9$. Results for $Wi > 0.6$ involve step changes in the rotation rate of the inner cylinder at $t = 4.5\lambda$, 8λ and 9.4λ.

appeared for $Wi > 0.6$, and hence for those results a time step of $\Delta t = 0.05\lambda$ was used. Since increasing the Weissenberg number corresponds to increasing either the relaxation time λ or the rotational velocity Ω, it is understandable that a smaller time step becomes necessary for larger Wi. Even with the smaller time step, moving to the final steady conditions at $Wi > 0.6$ was more stable when done in stages than when going from rest to $Wi > 0.7$ in one jump. Increasing the rotation rate in stages also served the purpose of showing the transient response of the method to changes made during a simulation. For $Wi > 0.6$, the rotation rate was increased from rest to $Wi = 0.6$ at $t = 0$, and further changes in rotation rate were used to increase the Weissenberg number at $t = 4.5\lambda$, 8λ and 9.4λ.

It is noted above that, to avoid the spreading of a dipolar blob through an interface confining the flow, interactions between dipoles and points on the surface of the journal bearing were not smoothed by the use of cutoff functions. As a result, the velocity on the cylinder surfaces to which the singularities external to the flow respond is slightly different than the velocity sensed by a dipole close to the surface. The magnitude of the radial velocity $v_r/\Omega R_0$ at $t = 5\lambda$ is plotted versus the cutoff parameter δ_c in figure 6 for three Weissenberg numbers, $Wi = 0.2, 0.4$ and 0.6. The size of the error, or the difference between the smoothed and unsmoothed velocity incurred at the boundary, is seen to be quite small, and it decreases linearly with decreasing δ_c. This rate of decrease is in contrast to the error estimates for e_d and e_m in (40), which show a δ_c^2 dependence for the error in the absence of boundary effects. It is in part because of this relatively strong dependence on δ_c contributed at the boundary that higher-order cutoff functions, such as the fourth-order cutoff given in (42), do not appear to offer any significant advantage in a surface-dominated lubrication flow such as this one. An improved rate of convergence, say δ_c^2 or higher, could presumably be obtained by using a smoothing procedure and cutoff functions that are not isotropic, and that explicitly account for the presence of the boundary.

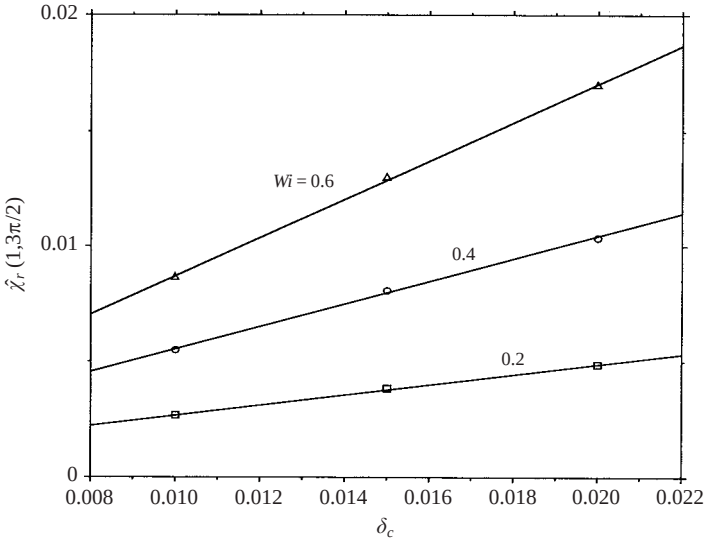

FIGURE 6. Error in the radial velocity $\hat{v}_r$ on the surface of the inner cylinder at $\theta = 3\pi/2$ for Weissenberg numbers of 0.2, 0.4 and 0.6. The error decreases linearly as the cutoff parameter δ_c is decreased.

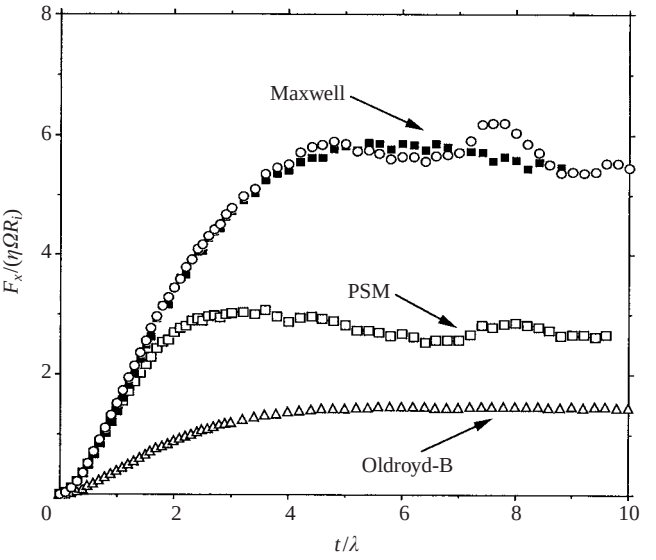

FIGURE 7. Simulation results for the x-directed force on the inner cylinder are shown at $Wi = 0.5$ for three constitutive models: the convected Maxwell constitutive model, the Oldroyd-B model With $S = 0.75$, and the PSM model with $\alpha = 10.0$. Results for the Maxwell model correspond to $N_d = 41\,353$ (open circles) and $N_d = 166\,096$ (solid squares).

Results for $F_x/\eta_0\Omega R_0$ for a convected Maxwell fluid, an Oldroyd-B fluid with $S = 0.75$, and a PSM fluid with $\alpha = 10.0$ are shown in figure 7 for $Wi = 0.5$. These values of S and α were chosen because they are representative of values found in the literature (Rajagopalan *et al.* 1993; Barakos & Mitsoulis 1995). Corresponding values of the y-component of force and the torque on the inner cylinder are given in

Constitutive model	$\frac{F_y}{\eta_0 \Omega R_i}$	$\frac{L_z}{\eta_0 \Omega R_i^2}$
Newtonian	164.3	67.9
Convected Maxwell	164.5	67.8
Oldroyd-B ($S = 0.75$)	164.9	68.0
PSM ($\alpha = 10.0$)	117.0	59.3

TABLE 2. Forces and torques for different constitutive models.

table 2. The effect of the solvent contribution described by S and the shear thinning of the first normal stress difference in the PSM model are clearly evident. For the Maxwell fluid and Oldroyd-B fluids, the normal stresses contribute a force in the x-direction, but there is a negligible effect on either the torque or y-component of force on the inner cylinder. The Oldroyd-B fluid's normal stresses are one-quarter that of the Maxwell fluid, because 75% of the viscous response of the Oldroyd-B fluid is contributed by the solvent. For the PSM fluid, shear thinning is present in both the normal stress coefficient and the shear viscosity. Hence, even though the zero-shear viscosity of the PSM fluid is the same as that of the Maxwell fluid, the x-component of force on the inner cylinder is significantly smaller. In addition, the torque on the rotating inner cylinder is also reduced significantly, because of the shear thinning viscosity. It is worth noting that it is quite easy to switch from one model to another, since the quantities needed to apply (11) with $S \neq 0$, or (14), are also known even if it is the relatively simple convected Maxwell model that is being used.

To evaluate the method further, calculations were performed at $Wi = 0.4$ for a range of eccentricities, $0.1 \leqslant \varepsilon \leqslant 0.4$. With the exception of the result at $\varepsilon = 0.4$, these calculations were also calculated with 41 353 dipoles, introducing new populations at time intervals of 3.6λ. As shown in figure 8, the results for $\varepsilon < 0.4$ are stable and accurate, with minimal fluctuations. At $\varepsilon = 0.4$, the width of the annulus in its thinnest region was too narrow relative to the dipole spacing, and the simulation did not reach a steady solution. Doubling the number of dipoles to 79 447 did yield a steady solution, although the fluctuations are pronounced, particularly at $t = 7.2\lambda$ where the third dipole population is introduced. That the fluctuation at $t = 7.2\lambda$ is a result of the change in dipole populations was confirmed by performing a simulation with 165 470 dipoles, in which only a single dipole population was used. The fluctuation has disappeared and the response is relatively smooth, but the simulation becomes unstable at approximately $t = 8\lambda$, as evidenced by the rapid drop in the x-component of force.

The eccentric cylinder configuration of figure 1 with an eccentricity of $\varepsilon = 0.4$ is quite different from the nearly uniform channel present at $\varepsilon = 0.1$. At the higher eccentricity, the ratio of wide-to-narrow dimension of the channel is 2.3:1, and a recirculation zone develops near the outer cylinder in the wide portion of the channel. This zone is clearly evident in contour plots of the angular velocity $\hat{v}_\theta$, presented in figures 9(a) and 9(b). These plots were made by using the conversion $(r, \theta) \rightarrow (\zeta, \theta)$, thereby mapping the flow domain to an annulus between concentric cylinders (Beris *et al.* 1983). The r- and ζ-coordinates are related by

$$\hat{r} = 1 + (\zeta - 1)(1 + \varepsilon \cos\theta) + O(\varepsilon^2 \mu^2). \tag{51}$$

In figure 9(a) the Newtonian velocity profile is shown, and figure 9(b) shows the result

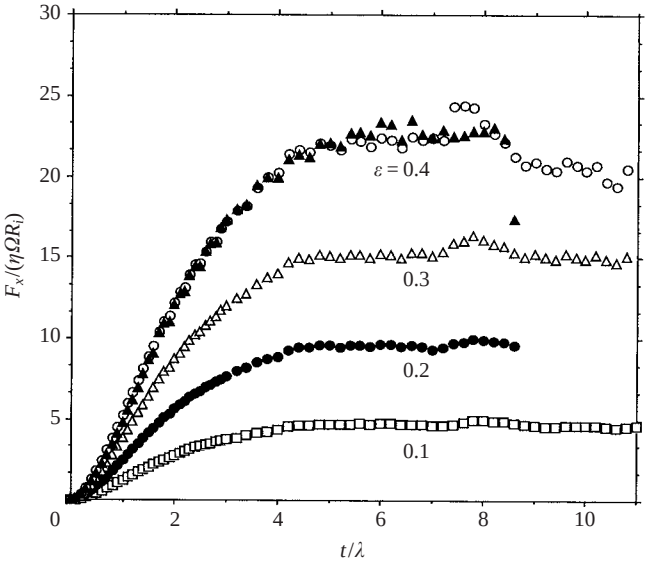

FIGURE 8. Simulation results for the x-directed force on the inner cylinder obtained with the convected Maxwell constitutive model are shown at $Wi = 0.4$ for eccentricities in the range $0 < \varepsilon \leqslant 0.4$. Results at $\varepsilon = 0.4$ correspond to $N_d = 79\,447$ (open circles) and $N_d = 165\,470$ (solid triangles).

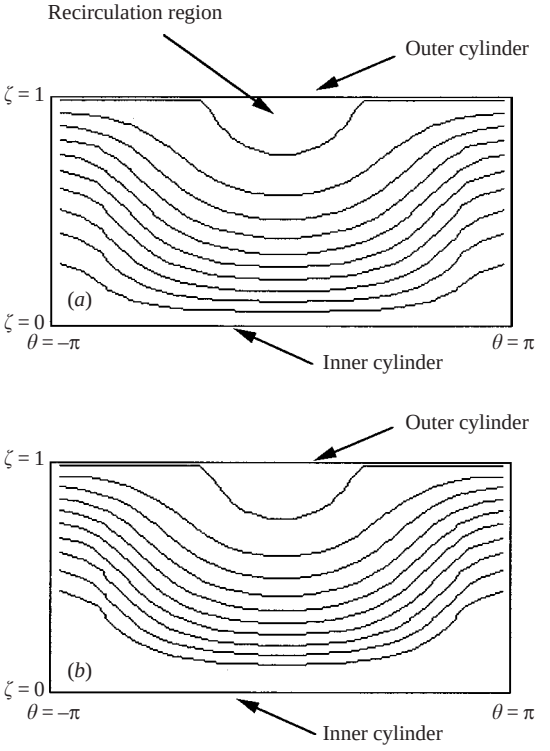

FIGURE 9. Contour plots of the velocity $\hat{v}_\theta$ obtained by using (*a*) a Newtonian constitutive model and (*b*) the convected Maxwell model at $Wi = 0.4$. The contour bounding the recirculation region corresponds to $\hat{v}_\theta = 0$, and that at the inner cylinder to $\hat{v}_\theta = 1$.

at $Wi = 0.4$. The recirculation zone in the wide region of the flow is bounded by the contour for which $\hat{v}_\theta = 0$, and is identified on the plot.

In fact, the Newtonian and non-Newtonian velocity fields should be indistinguishable for the convected Maxwell model in this geometry, as has been found by others (Beris, Armstrong & Brown 1986). This result is also obtained with the current method in most of the flow domain, but the contours do show a change near the inner rotating cylinder, where they are farther from the surface for the non-Newtonian flow than for the Newtonian flow. Since the non-Newtonian stresses in the flow are significant, as evidenced by the results for the force on the cylinder, these plots show that the non-zero contributions of the dipoles to the velocity field cancel one another as they should, leaving the net flow almost unchanged. In addition, one sees that the smoothing process described in § 3.1 does allow one to calculate velocity fields throughout the fluid, even though it contains point-dipole singularities. These velocity profiles show some fluctuations as a result of those singularities, but the fluctuations are small, being about 1% of the overall strength of the flow in this case. The radial component of the velocity is quite weak in these flows, and is smaller than 1% of the angular velocity. Hence, meaningful contour plots of the radial velocity could not be produced.

4.2. *Shear thinning in a wide-gap concentric-cylinder geometry*

In order to examine a case where strong shear thinning is present, and where analytical results are also available for comparison, additional calculations were made for a power-law fluid flowing in a concentric-cylinder geometry with a wide gap. The inner and outer radii were in the ratio $R_0/R_i = 1.4$, and the constitutive equation was given by

$$\tau^\pi = (m|\dot{\gamma}|^{n-1} - \mu)\dot{\gamma}, \tag{52}$$

where n is the flow index, and shear thinning is present for $n < 1$. The velocity profile for a power-law fluid flowing between concentric cylinders, with the inner cylinder rotating, is

$$\hat{v}_\theta = \left[\frac{(1/\hat{r})^{2/n} - 1}{(R_0/R_i)^{2/n} - 1}\right]\hat{r}, \tag{53}$$

and the torque per unit length on the inner cylinder by

$$\hat{L}_z = 2\pi\left[\frac{2/n}{1 - (R_i/R_0)^{2/n}}\right]^n. \tag{54}$$

Velocity profiles are shown in figure 10 for values of the flow index in the range $0.3 < n < 1$, where $n = 0.3$ corresponds to a strongly shear-thinning fluid. The solid curves are the predictions of (53), and the data points are results from the PDM. With 29 304 dipoles, excellent agreement is obtained at $n = 0.6$, and the predicted velocity is in error by approximately 6% at $n = 0.4$. Note that, as the width of the gap increases from $0.11R_i$ to $0.4R_i$, the number of dipoles needed to fill the domain decreases, because the disparity in length scales between the radial and angular directions is decreased. Doubling the number of dipoles from 29 304 to 60 164 yields excellent agreement at $n = 0.4$, with only slight errors present for $1 < \hat{r} < 1.1$, where the velocity gradient is quite steep. At $n = 0.3$, agreement is still good, but the errors close to the inner cylinder increase to approximately 6%. Even at $n = 0.3$, the torques given by the PDM are very accurate, differing from (54) by only 0.1%.

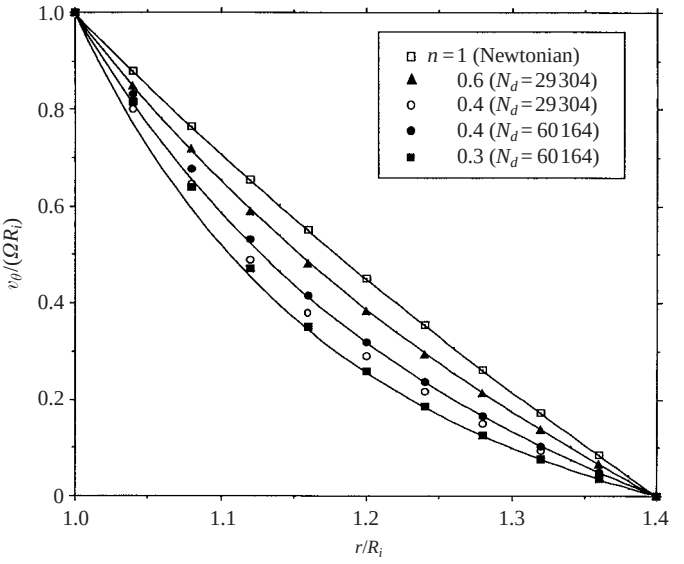

FIGURE 10. Plots of the angular velocity vs. radial position for flow of a power-law fluid between concentric cylinders, with $R_0/R_i = 1.4$, calculated by using the point-dipole method. Results are shown for values of the flow index n in the range $0.3 \leqslant n \leqslant 1.0$.

4.3. *Two-phase oscillatory flow between concentric cylinders*

An interesting and useful characteristic of the PDM is the Lagrangian nature of the dipoles, which always move with the surrounding fluid. Because of this trait, the method is well-suited to simulations of moving particles, which can be represented as clusters of singularities, or to simulating two-phase flows of immiscible liquids. In the wide-gap concentric-cylinder geometry, we have used this feature to study time-dependent flow of a viscoelastic fluid in contact with a Newtonian fluid. The viscosity of the Newtonian fluid is the same as that of the viscoelastic fluid, which is described by the convected Maxwell model (and hence does not shear thin). A schematic diagram of the situation is shown in figure 11. The annulus is half-filled with a Newtonian fluid, which is on the bottom, and the top half is filled with a viscoelastic fluid. The densities of the two fluids and the surface tension at the interface are such that buoyancy effects and capillarity are negligible relative to viscous effects.

We note that, using the methods recently developed by Nitsche & Schaflinger (2001), in which point forces rather than dipoles are distributed throughout a fluid, both unequal densities and surface tension could be included within the framework of this singularity method. In addition, by using the point forces in the fluid to account for inertial forces, and Green's function for the unsteady Stokes equations instead of (7) (cf. Pozrikidis 1992), the method could be extended to finite Reynolds numbers. However, we have not included those effects here.

Hence, in the current problem, representing the Newtonian fluid is as simple as removing the dipoles from the lower half of the flow domain. The fluid interface is taken to be flat initially, and then at $t = 0$ the inner cylinder begins to rotate with a sinusoidal velocity:

$$\hat{v}_\theta(\hat{r} = 1) = \sin \hat{\omega}\hat{t}, \tag{55}$$

where the frequency has been non-dimensionalized by the relaxation time λ, and the angular velocity by the product of the maximum rotation rate and the inner radius

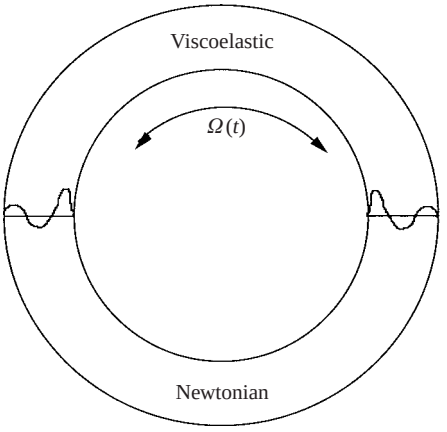

FIGURE 11. Schematic diagram of a time-dependent two-phase flow between concentric cylinders with $R_0/R_i = 1.4$. The viscoelastic fluid is on top ($y > 0$), a Newtonian fluid with the same density and viscosity is underneath, and the inner cylinder rotates with velocity $\Omega(t)$.

R_i. If the Deborah and Weissenberg numbers are defined as in (3) and (4), but with Ω being the maximum rotation rate, then the values for this time-dependent simulation are $Wi = 0.3$ and $De = 0.12$. The dimensionless frequency is $\hat{\omega} = \pi/6$, so that one cycle is completed at dimensionless time intervals of 12. The number of dipoles was 14 606, lower than is used in the examples above because half of the annulus is filled with dipole-free Newtonian fluid. The interface between the two liquids is tracked by 100 points that initially form a horizontal line at $y = 0$, and thereafter move with the fluid, but play no other role in the simulation.

The position of this interface is plotted in figure 12(a) for the left-hand side of the annulus (cf. figure 11), and in figure 12(b) for the right-hand side. The positions plotted correspond to times of 3, 6 and 9 cycles, or $t = 12\lambda$, 24λ and 36λ. For a pure Newtonian fluid, the interface would necessarily remain flat, as a consequence of the reversibility of Stokes equations. As shown, when the upper fluid is viscoelastic, the Newtonian fluid is pulled upward, particularly along the surface of the inner cylinder. The motion is not symmetric, with the left- and right-hand sides showing significant differences, although the Newtonian fluid is pulled upward in each case. The protrusion of Newtonian fluid on the right-hand side is broader than that on the left, and shows two pronounced peaks relative to only one on the left. This asymmetry is to be expected because the left- and right-hand interfaces are significantly different: on the left-hand side, the rotation of the cylinder moves viscoelastic fluid into Newtonian fluid, whereas on the right it moves Newtonian fluid into viscoelastic fluid.

The results, denoted by open circles, open squares and solid triangles, after 3, 6 and 9 cycles, respectively, correspond to a cutoff parameter set at $\delta_c = 0.036$. In these cases, both the dipole velocities and the velocities of the points marking the liquid/liquid interface were calculated using this value. At 9 cycles, a set of results is also shown in figure 12(a, b) where dipole–dipole interactions are smoothed in the usual manner, with $\delta_c = 0.036$, but the velocities used to update the interface position were not smoothed. These points, denoted by solid circles, are labelled $\delta_c = 0$. The interface shape they show (the solid circles) is qualitatively identical to those marked $\delta_c = 0.036$ (the solid triangles), but is shifted downward significantly and the points are relatively scattered. As mentioned above, the velocity field generated by

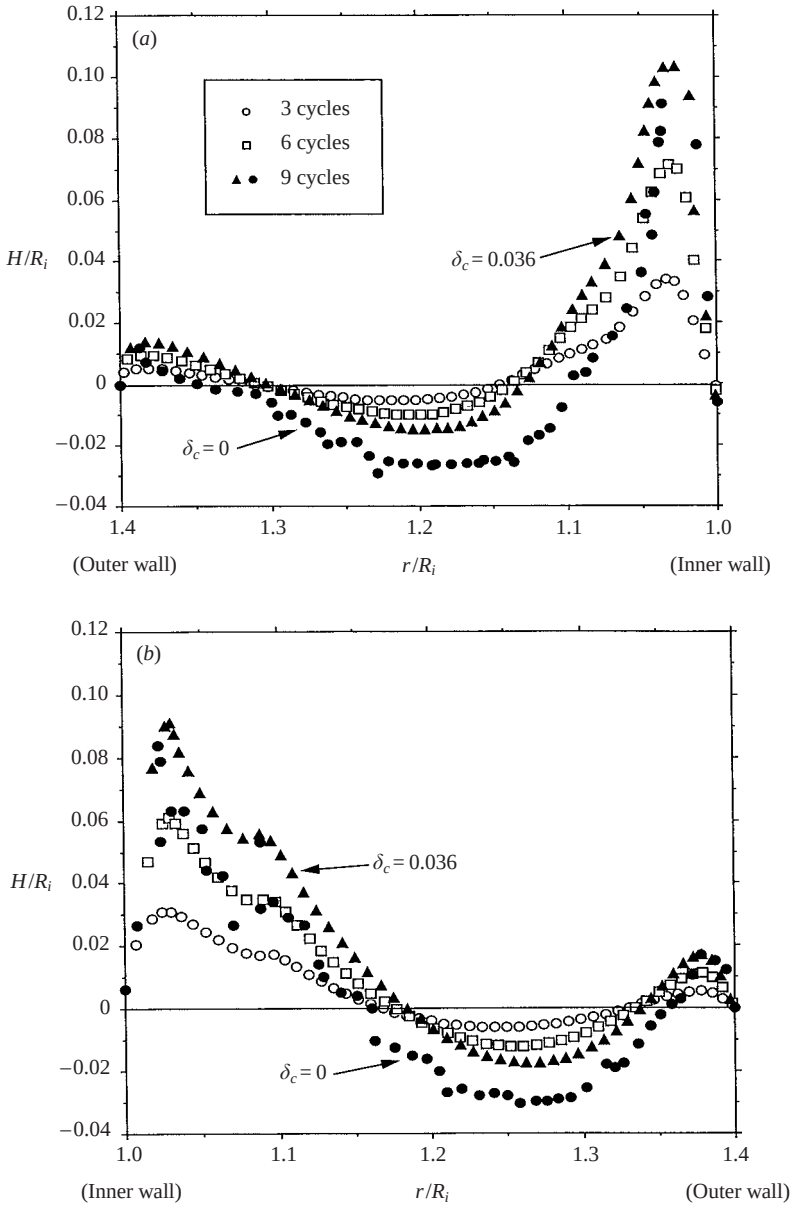

FIGURE 12. Positions of the interface on (*a*) the left-hand side and (*b*) the right-hand side for the configuration shown in figure 11, after the inner cylinder has completed 3, 6 and 9 cycles. At 9 cycles, results are shown for interface positions updated with the smoothed ($\delta_c = 0.036$) and unsmoothed ($\delta_c = 0$) propagator. A cycle corresponds to a time of 12λ.

the smoothed dipole propagator $\nabla \boldsymbol{J}_\delta$ only conserves mass exactly for distances far from the dipole relative to δ_c, and the use of $\nabla \boldsymbol{J}_\delta$ near a liquid/liquid interface can therefore cause a net increase or decrease of the two phases. In contrast, changes in interface positions computed with the unsmoothed propagator $\nabla \boldsymbol{J}$, corresponding to $\delta_c = 0$, are irregular but conserve mass exactly. Figure 12(*a*, *b*), shows that for the interface changes computed with $\delta_c = 0.036$ there is a net increase in Newtonian fluid,

with the parts of the interface displaced upward moving farther than those moving downward. This undesirable effect is absent in the interface marked $\delta_c = 0$.

The behaviour of the interface can be explained qualitatively. In a two-dimensional flow, a normal stress difference can be thought of as a tension along the streamlines (Barnes, Hutton & Walters 1989). Hence, there is a tension in the upper viscoelastic fluid that is not present in the lower Newtonian fluid. That tension is greatest where the shear rate is greatest, close to the inner cylinder, and hence Newtonian fluid is pulled upward there. The requirement that mass be conserved then results in a reverse pressure-driven flow of viscoelastic fluid into the Newtonian region, and this flow is strongest in the middle of the channel. Apparently the pressure-driven flow is not able to overcome the normal-stress-driven tension near the outer cylinder wall, and so a second protrusion of Newtonian fluid into the upper viscoelastic region is found there. This explanation does not explain the bimodal shape of the interface on the right-hand side, but it does provide a simple interpretation of the overall behaviour. There appear to be no experimental results available for comparison with these results.

5. Conclusion

A new method has been introduced for calculating time-dependent viscoelastic flows with integral constitutive equations. The method is based on the integral solution to the equations of motion in the limit of low Reynolds number, but differs from the well-known boundary-integral method because of nonlinear terms required by the non-Newtonian nature of the flow. The method has been shown to be accurate at low and moderate levels of elasticity, or when $Wi < 1$, and in the presence of strong shear thinning, such that the flow index is in the range $0.3 \leqslant n \leqslant 1$. The method can be readily applied to any integral (or algebraic) constitutive equation. Hence, it allows one to take full advantage of the ability of such models to account for the multiple relaxation times present in most viscoelastic fluids, as well as other advantages they might offer in capturing realistic rheological properties. In addition, the fact that the dipoles contributing the non-Newtonian stresses in the flow are Lagrangian in nature, and move with the fluid velocity, makes the method well-suited to multiphase flow calculations or particle dynamics simulations involving non-Newtonian fluids.

This work was funded by NSF Grant CTS 98126. Partial funding was also provided by Grant 36065-AC9 from the American Chemical Society Petroleum Research Fund (ACS-PRF).

REFERENCES

Anderson, C. & Greengard, C. 1985 On vortex methods. *SIAM J. Numer. Anal.* **22**, 413–440.

Ballal, B. Y. & Rivlin, R. S. 1976 Flow of a viscoelastic fluid between eccentric rotating cylinders. *Trans. Soc. Rheol.* **20**, 65–101.

Barakos, G. & Mitsoulis, E. 1995 Numerical simulation of viscoelastic flow around a cylinder using an integral constitutive equation. *J. Rheol.* **39**, 1279–1292.

Barnes, H. A., Hutton, J. F. & Walters, K. 1989 *An Introduction to Rheology*. Elsevier.

Batchelor, G. K. 1970 Slender-body theory for particles of arbitrary cross-section in Stokes flow. *J. Fluid Mech.* **44**, 419–440.

Beris, A., Armstrong, R. C. & Brown, R. A. 1983 Perturbation theory for viscoelastic fluids between eccentric rotating cylinders. *J. Non-Newtonian Fluid Mech.* **13**, 109–148.

Beris, A., Armstrong, R. C. & Brown, R. A. 1986 Finite element calculation of viscoelastic flow in a journal bearing; II. Moderate eccentricity. *J. Non-Newtonian Fluid Mech.* **19**, 323–347.

Bird, R. B. B., Armstrong, R. C. & Hassager, O. 1987*a* *Dynamics of Polymeric Liquids. 1. Fluid Mechanics*. Wiley.

Bird, R. B. B., Curtiss, C. F., Armstrong, R. C. & Hassager, O. 1987*b* *Dynamics of Polymeric Liquids. 2. Kinetic Theory*. Wiley.

Binous, H. & Phillips, R. J. 1999*a* Dynamic simulation of one and two particles sedimenting in viscoelastic suspensions of FENE dumbbells. *J. Non-Newtonian Fluid Mech.* **83**, 93–130.

Binous, H. & Phillips, R. J. 1999*b* The effect of sphere-wall interactions on particle motion in a viscoelastic suspension of FENE dumbbells. *J. Non-Newtonian Fluid Mech.* **85**, 63–92.

Board, J. A., Causey, J. W., Leathrum, J. F., Windemuth, A. & Schulten, K. 1992 Accelerated molecular dynamics simulation with the parallel fast multipole algorithm. *Chem. Phys. Lett.* **198**, 89–94.

Buck, K. S., Dungan, S. R. & Phillips, R. J. 1999 The effect of solute concentration on hindered gradient diffusion in polymeric gels. *J. Fluid Mech.* **396**, 287–317.

Chawda, A. & Avgousti, M. 1996 Stability of viscoelastic flow between eccentric rotating cylinders. *J. Non-Newtonian Fluid Mech.* **63**, 97–120.

Choi, C. H., Ruedenberg, K. & Gordon, M. S. 2001 New parallel optimal-parameter fast multipole method. *J. Comput Chem.* **22**, 1484–1501.

Chorin, A. J. & Marsden, J. E. 1993 *A Mathematical Introduction to Fluid Mechanics*. Springer.

Chung, T. J. 1978 *Finite Element Analysis in Fluid Dynamics*. McGraw-Hill.

Chwang, A. T. & Wu, T. Y. 1975 Hydromechanics of low-Reynolds number flow. Part 2. Singularity method for Stokes flows. *J. Fluid Mech.* **67**, 787–815.

Clague, D. S. & Phillips, R. J. 1996 Hindered diffusion of spherical macromolecules through dilute fibrous media. *Phys. Fluids* **8**, 1720–1730.

Clague, D. S. & Phillips, R. J. 1997 A numerical calculation of the hydraulic permeability of three-dimensional disordered fibrous media. *Phys. Fluids* **9**, 1562–1572.

Cox, R. G. 1970 The motion of long slender bodies in a viscous fluid. Part 1. General theory. *J. Fluid Mech.* **44**, 791–810.

Dabros, T. 1985 A singularity method for calculating hydrodynamic forces and particle velocities in low-Reynolds-number flows. *J. Fluid Mech.* **156**, 1–21.

Dris, I. M. & Shaqfeh, E. S. G. 1998 Experimental and theoretical observations of elastic instabilities in eccentric cylinder flows: local versus global instability. *J. Non-Newtonian Fluid Mech.* **80**, 1–58.

Goodman, J., Hou, T. Y. & Lowengrub, J. 1990 The convergence of the point vortex method for the 2-D Euler equations. *Commun. Pure Appl. Maths* **43**, 415–430.

Greengard, L. 1988 *The Rapid Evaluation of Potential Fields in Particle Systems*. MIT Press.

Greengard, L. & Gropp, W. D. 1990 A parallel version of the fast multipole method. *Computers Maths with Applics.* **20**, 63–71.

Greengard, L. & Rokhlin, V. 1997 A fast algorithm for particle simulations. *J. Comput Phys.* **135**, 280–292.

Grillet, A. M., Lee, A. G. & Shaqfeh, E. S. G. 1999 Observations of ribbing instabilities in elastic fluid flows with gravity stabilization. *J. Fluid Mech.* **399**, 49–83.

Jackson, J. D. 1975 *Classical Electrodynamics*. Wiley.

Kim, S. 1986 Singularity solutions for ellipsoids in low-Reynolds number flows: With applications to the calculation of hydrodynamic interactions in suspensions of ellipsoids. *Intl J. Multiphase Flow* **12**, 469–491.

Ladyzhenskaya, O. A. 1969 *The Mathematical Theory of Viscous Incompressible Flow*. Gordon and Breach.

Larson, R. G., Muller, S. J. & Shaqfeh, E. S. G. 1994 The effect of fluid rheology on the elastic Taylor–Couette instability. *J. Non-Newtonian Fluid Mech.* **51**, 195–225.

Larson, R. G., Shaqfeh, E. S. G. & Muller, S. J. 1990 A purely elastic instability in Taylor–Couette flow. *J. Fluid Mech.* **218**, 573–600.

Lee, J. Y. & Jeong, K. 1998 A parallel Poisson solver using the fast multipole method on networks of workstations. *Computers Maths with Applics.* **36**, 47–61.

Nitsche, L. C. & Brenner, H. 1990 Hydrodynamics of particle motion in sinusoidal pores via a singularity method. *AIChE J.* **36**, 1403–1419.

Nitsche, L. C. & Schaflinger, U. 2001 A swarm of Stokeslets with interfacial tension. *Phys. Fluids* **13**, 1549–1553.

Papanastasiou, A. C., Scriven, L. E. & Macosko, C. W. 1983 An integral constitutive equation for mixed flows: Viscoelastic characterization. *J. Rheol.* **27**, 387–748.

Peters, E. A. J. F., Hulsen, M. A. & van den Brule, B. H. A. A. 2000 Instationary Eulerian viscoelastic flow simulations using time separable Rivlin–Sawyers constitutive equations. *J. Non-Newtonian Fluid Mech.* **89**, 209–228.

Phan-Thien, N. & Tanner, R. I. 1981 Journal lubrication and normal stress measurement. *J. Non-Newtonian Fluid Mech.* **9**, 107–117.

Phillips, R. J. 1995 Calculation of multisphere linearized Poisson–Boltzmann interactions near cylindrical fibers and planar surfaces. *J. Colloid Interface Sci.* **175**, 386–399.

Pozrikidis, C. 1992 *Boundary Integral and Singularity Methods for Linearized Viscous Flow*. Cambridge University Press.

Puckett, E. G. 1993 Vortex methods: an introduction and survey of selected research topics. In *Incompressible Computational Fluid Dynamics* (ed. M. D. Gunzburger, R. A. Nicolaides). Cambridge University Press.

Rajagopalan, D., Armstrong, R. C. & Brown, R. A. 1993 Comparison of computational efficiency of flow simulations with multimode constitutive equations: integral and differential models. *J. Non-Newtonian Fluid Mech.* **46**, 243–273.

Rasmussen, H. 1999 Time-dependent finite-element method for the simulation of three-dimensional viscoelastic flow with integral models. *J. Non-Newtonian Fluid Mech.* **84**, 217–232.

Sangani, A. S. & Mo, G. 1996 An $O(N)$ algorithm for Stokes and Laplace interactions of particles. *Phys. Fluids* **8**, 1990–2010.

Tanner, R. I. 1992 *Engineering Rheology*. Oxford University Press.

Zheng, R., Phan-Thien, N., Tanner, R. I. & Bush, M. B. 1990 Numerical analysis of viscoelastic flow through a sinusoidally corrugated tube using a boundary element method. *J. Rheol.* **34**, 79–102.